



# Damage evolution in coal under different loading modes using advanced digital volume correlation based on X-ray computed tomography

Haizhou Liu, Lingtao Mao, Yang Ju, François Hild

## ► To cite this version:

Haizhou Liu, Lingtao Mao, Yang Ju, François Hild. Damage evolution in coal under different loading modes using advanced digital volume correlation based on X-ray computed tomography. *Energy*, 2023, 275, pp.127447. 10.1016/j.energy.2023.127447 . hal-04216100

**HAL Id: hal-04216100**

**<https://hal.science/hal-04216100>**

Submitted on 23 Sep 2023

**HAL** is a multi-disciplinary open access archive for the deposit and dissemination of scientific research documents, whether they are published or not. The documents may come from teaching and research institutions in France or abroad, or from public or private research centers.

L'archive ouverte pluridisciplinaire **HAL**, est destinée au dépôt et à la diffusion de documents scientifiques de niveau recherche, publiés ou non, émanant des établissements d'enseignement et de recherche français ou étrangers, des laboratoires publics ou privés.

**Damage evolution in coal under different loading modes using advanced digital volume correlation based on X-ray computed tomography**

Haizhou Liu,<sup>1,2</sup> Lingtao Mao,<sup>1,3,\*</sup> Yang Ju<sup>1,3</sup>, and François Hild<sup>2</sup>

<sup>1</sup> *School of Mechanics and Civil Engineering, China University of Mining & Technology, Beijing 100083, China*

<sup>2</sup> *Université Paris-Saclay, CentraleSupélec, ENS Paris-Saclay, CNRS*

*LMPS - Laboratoire de Mécanique Paris-Saclay, 91190 Gif-sur-Yvette, France*

<sup>3</sup> *State Key Laboratory of Coal Resources and Safe Mining, China University of Mining & Technology, Beijing 100083, China*

\*Corresponding author: Lingtao Mao, E-mail: [mlt@cumtb.edu.cn](mailto:mlt@cumtb.edu.cn)

## **Highlights**

- Microscale nascent fractures at sub-voxel resolutions of coal were evaluated.
- Fracture developments were revealed by fracture closure/opening displacements.
- Element-based damage growth was assessed by advanced DVC at a very fine mesh scale.
- Fracture-related parameters were counted based on refined fracture identification.

## Abstract

To investigate the damage development of coal under different loading conditions, *in-situ* tests in uniaxial and triaxial compression were carried out. Advanced digital volume correlation based on finite element discretization was utilized to quantify the three-dimensional initial and newborn fractures. With this technique, the low contrast in the coal images was compensated for by mechanical regularization, and the fracture activities were quantified via a damage variable and mesh refinement scheme, including fracture opening/closure displacements, volume fractions of damaged elements, and fractal dimensions. The experiments revealed that the damage growth in coal was substantially affected by randomly distributed initial defects. Prior to a macroscopic failure, the coal samples generally experienced pre-existing fracture closure, newborn fracture initiation, interaction and propagation of the two fracture types. This study aimed to gain in-depth insights into the bulk fracture of coal and provide quantitative evidence for further understanding the damage mechanisms from the microscale to the macroscale.

**Keywords:** Damage, Coal, Compression, Digital volume correlation, X-ray computed tomography

## 1. Introduction

As a fossil fuel with the most abundant reserves on Earth, coal accounts for more than 50% of the total global fossil fuel, supporting economic and social development [1]. With the rapid increase in demand for energy, special attention is increasingly paid to deep mining owing to the near depletion of shallow coal resources [2]. However, the stress environment becomes highly complex with an increased depth of the buried coal seam [3]. In particular, for fractures that typically provide a network and pathway for gas or fluid transport [4]. In addition, the increased stress disturbance in deep mining may cause internal damage to coal at the end of the working face, which could increase the frequency of hazards, such as coal-gas outburst disasters [5].

Coal is composed of a various mineral crystal particles, such as quartz, clay, feldspar and carbonates [6], thereby inducing heterogeneity and anisotropy. Coal is a complex medium with randomly distributed initial defects, which are natural damage sites that may expand, interconnect and eventually coalesce to generate macroscopic fractures under external loading conditions [7]. The damage growth from such defects and their inhomogeneous distributions may considerably affect the mechanical properties of coal under different loading conditions. Therefore, a better understanding and quantification of damage and fracture features of coal are of great interest to the elucidation and control of the various failure mechanisms.

Given the limitations of experimental equipment and technical conditions, accurately quantifying the mechanical parameters and damage characteristics of coal via traditional fracture tests is difficult [8-10]. In recent years, combined with image processing technology, high resolution X-ray computed tomography (XCT) scanners have been adopted to characterize the internal microstructure and damage development of coal under different loading conditions [11-14]. Zhou et al. [15] studied the characteristics of fracture networks at different measurement resolutions under uniaxial compression. Wu et al. [16] quantitatively analyzed the meso-damage growth and fracturing characteristics of coal under uniaxial compression by using the theory of gray level co-occurrence matrix. Shi et al. [17] characterized the permeability of bituminous coal under *in-situ* steam pyrolysis. Sun et al. [18]

1 estimated the growth of pores and fractures during the spontaneous combustion of coal in  
2 changing temperature and gas atmosphere. In addition to the afore mentioned direct analyses  
3 of CT images, reconstructed volumes with real microstructures of coal were also used to  
4 model the mechanical response to varying loading condition. Wang et al. [19] simulated  
5 water injection and deformative coal under uniaxial compression via a finite element (FE)  
6 method using the industrial LS-DYNA code. Zhong et al. [20] performed numerical  
7 simulations of coal under uniaxial and triaxial compression and qualitatively analyzed  
8 damage growth. Zheng et al. [21] investigated the dynamic response and effect of the  
9 mesostructure on the fracture mechanism of heterogeneous coal-rock using the discrete  
10 element method combined with CT images.

11 Although the damage growth of coal has been roughly estimated, other tools still need to  
12 be developed to quantify the internal deformation to provide detailed understanding of the  
13 damage mechanisms. Among the various image processing techniques, digital volume  
14 correlation (DVC) has emerged as a powerful tool for measuring displacement fields based  
15 on FE discretization of XCT images [22, 23]. This method has been used on many materials,  
16 such as bones [24], polymers [25], concrete [26] and sandstone [27]. To the best of our  
17 knowledge, there exist only few studies on the application of DVC with coal. Mao et al. [28]  
18 used digital volumetric speckle photography (DVSP) (*i.e.*, subset-based DVC) in  
19 combination with CO<sub>2</sub> injection in coal to characterize long-term CO<sub>2</sub>-induced strains, which  
20 are heterogeneous and localized depending on microlithotype and microstructure. Wang et al.  
21 [29] performed a triaxial hydraulic fracturing test on coal and quantified fracture-related  
22 parameters (*i.e.*, structural variation and spatial distribution) to reveal the macroscopic  
23 development of fractures via image analysis technology. The displacement and strain fields  
24 after fracturing were also estimated using FE-based DVC to analyze the fracture  
25 characteristics. Vishal et al. [30] provided in-depth insights into crack initiation and  
26 propagation in coal subjected to incremental uniaxial loading. The dynamic changes in the  
27 coal matrix, permeability, and tortuosity under stress were detailed for different intervals. In  
28 particular, the behavior of the tensile and shear cracks was characterized by measuring the  
29 accumulated strain fields.

Owing to the afore mentioned contributions, the evolutionary characteristics of fractures have been investigated in detail. However, some limitations to the precise description of damage growth remain (or fracture evolution), which mainly focus on three aspects. First, fractures above the CT resolution were extracted using image processing techniques (*e.g.*, watershed segmentation), whereas, fracture openings below the CT resolution (*i.e.*, sub-voxel damage) were not identified. Second, the behavior of fractures was roughly revealed via the strain fields; however, intuitive quantities (*e.g.*, fracture opening/closure displacements) were not mentioned or measured during the entire loading history. Finally, in FE-based DVC, the mesh size and its corresponding measurement uncertainty are the essential factors for investigating element-based strains. As the mesh size is often greater than 20 vx in the standard FE-based DVC analysis (*e.g.*, Avizo software), precisely describing fractures on a small scale (*i.e.*, few voxels) is almost impossible.

This study aimed to quantify the fracture opening/closure displacements (FODs/FCDs) via an advanced DVC analysis over the entire loading history of coal under uniaxial *and* triaxial compression. Compared with previous DVC-based studies on coal fractures, the proposed DVC framework quantified the FODs/FCDs at sub-voxel resolution using extremely fine meshes (*i.e.*, 5 vx elements). The remainder of this study is organized as follows: Section 2 introduces experimental set-up and apparatus; Section 3 describes the research methods and fracture assessment parameters; and Section 4 presents the DVC results and related discussion.

## **2. Experimental set-up**

To study the development of coal fractures under different loading modes, two coal samples were prepared and subjected to in-situ XCT experiments in which uniaxial and triaxial compressive loadings were applied. An XCT scanning system and *in-situ* loading setups are shown in Fig. 1 and comprised several tightly connected components as follows: a field emission X-ray (FEX) source with 225 kV micro-focus, an array detector with a definition of  $1024 \times 1024$  pixels, a turntable, a scanning control station, a loading setup for uniaxial [31] or triaxial [32] compression, and its loading control system. In the experiment, the coal

samples were placed in homemade in-situ testing machines, which were rotated with the turntable of the XCT system during scans. X-rays penetrated the sample placed in the chamber, and transmitted intensity was monitored via a detector. A series of radiographic projections were acquired to reconstruct three-dimensional (3D) volumes [33]. The corresponding XCT hardware parameters are listed in Table 1.

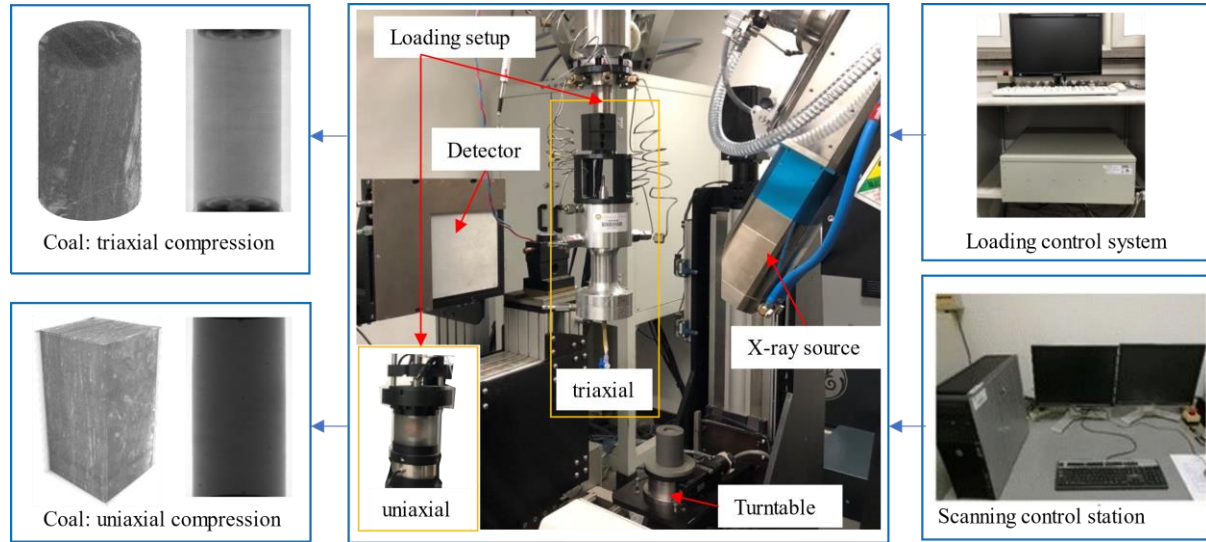


Fig. 1 X-ray computed tomography (XCT) scanning system for *in-situ* triaxial compressive tests

Table 1. XCT hardware parameters.

Experimental type	Uniaxial compression	Triaxial compression
X-ray source	YXLON	YXLON
Target / Anode	W (reflection mode)	W (reflection mode)
Voltage	110 kV	150 kV
Current	200 $\mu$ A	300 $\mu$ A
Focal spot size	$3 \times 6 \mu\text{m}$	$3 \times 6 \mu\text{m}$
Tube to detector	697 mm	697 mm
Tube to object	140 mm	190 mm
Detector	XRD 0822 AP14	XRD 0822 AP14
Definition	$1024 \times 1024$ pixels	$1024 \times 1024$ pixels
Number of projections	720	720
Angular amplitude	$360^\circ$	$360^\circ$



Frame average	No	No
Acquisition duration	25 min	25 min
Reconstruction algorithm	filtered back-projection	filtered back-projection
Gray levels amplitude	16 bits	16 bits
Volume size	$460 \times 460 \times 860$ vx (crop)	$\approx \Phi 440 \times 800$ vx (crop)
Field of view	$17.0 \times 17.0 \times 31.8$ mm <sup>3</sup> (crop)	$\approx \Phi 22 \times 40$ mm <sup>3</sup> (crop)
Image scale	37.0 $\mu$ m/ vx	50.0 $\mu$ m/ vx
Pattern	natural (Fig. 2(a))	natural (Fig. 2(b))

In this study, bulk coal was collected from the Yangquan coal mine in Shanxi Province, China. The composition was 0.98 vol% moisture, 18.61 vol% ash, 13.73 vol% volatile matter, and 66.8 vol% carbon. The coal samples were processed using wire cutting into the shapes of a cube ( $19 \times 19 \times 40$  mm<sup>3</sup>) for uniaxial compression, and a cylinder ( $\Phi 25 \times 50$  mm<sup>2</sup>) for triaxial compression. The chambers used in the uniaxial and triaxial set-ups were composed of plexiglass [34] and high-strength aluminum alloy [32], respectively. Each scan took approximately 25 min with a maintained applied force (Table 1). Figure 2 shows the 3D renderings after thresholding for the two coal samples to illustrate the microstructure heterogeneity and the corresponding gray level (GL) histograms in the reference configuration (*i.e.*, without any loading). Initial cracks and high-density inclusions were observed in the coal sample subjected to uniaxial compression. Conversely, layered distributions of low and high density components were present in the coal sample subjected to triaxial compression. The dynamic ranges in uniaxial and triaxial compression were approximately 2000 - 6000 GL and 1000 - 3000 GL, respectively. In addition, a stronger asymmetry of the gray level distribution was observed for the coal sample tested in triaxial compression.

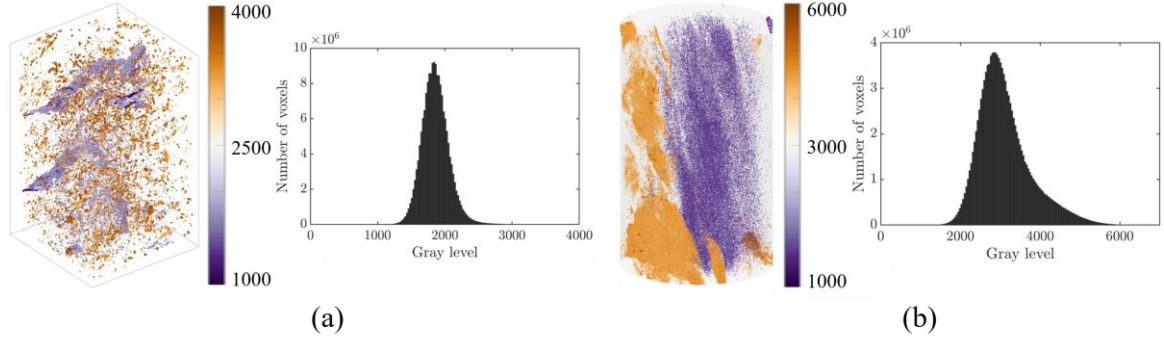


Fig. 2 3D renderings after thresholding of the tested samples and corresponding gray level histograms. (a) uniaxial and (b) triaxial compression.

To evaluate the image quality, the following four parameters related to the signal and noise are listed in Table 2: signal-to-noise ratio ( $SNR$ ), reflecting the noise level; contrast-to-noise ratio ( $CNR$ ), representing the contrast between signal and noise; gradient-to-noise ratio ( $GNR$ ), describing the gradient contrast between signal and noise; and root-mean-square contrast ( $C_\sigma$ ), denoting the signal quality. The four parameters of the sample tested were lower in triaxial compression than in axial compression. In other words, the quality of the former was poorer than that of the latter owing to the influence of the casing of the pressure cavity in the triaxial set-up (Fig. 2).

Table 2. Assessment parameters of image quality.

Parameter	Expression	Uniaxial	Triaxial
$SNR$	$SNR = 10\ln(\sigma_s^2/\sigma_n^2)$	8.7	3.1
$CNR$	$CNR = 10\ln( \mu_s - \mu_n /\sqrt{\sigma_s^2 + \sigma_n^2})$	8.3	-4.4
$GNR$	$GNR = 10\ln[(rms)_{gs}^2/(rms)_{gn}^2]$	13.7	-0.4
$C_\sigma$	$C_\sigma = rms[(I_s - \mu_s)/I_s]$	2.6	1.5

Notation:  $\mu_s$  ( $\mu_n$ ) and  $\sigma_s$  ( $\sigma_n$ ) are the mean and standard deviation of the gray levels within the samples (the surrounding air), respectively;  $(rms)_{gs}$  and  $(rms)_{gn}$  are the root-mean-square of the gray-level gradient in the sample and noise gradient, respectively; and  $I_s$  is the gray level of the sample.

### 3. Methods and assessment parameters

#### 3.1 Regularized multi-mesh damaged-DVC (RMD-DVC) framework

The general goal of FE-based global DVC [35] is to determine the voxel-based displacement fields  $u(x, \{v\})$  between the reference volume  $f$  and deformed volume  $g$ , by minimizing the sum of squared differences  $\Phi_c^2(\{v\})$  over the region of interest (ROI) as follows:

$$\Phi_c^2(\{v\}) = \sum_{ROI} \|f(x) - g(x + u(x, \{v\}))\|^2 \quad (1)$$

where the sought displacement field is parameterized in a FE sense is as follows:

$$u(x, \{v\}) = \sum_i v_i \phi_i(x) \quad (2)$$

where  $\phi_i(x)$  is the shape function associated with the nodal displacement  $v_i$  to be measured, which is collected in the column vector  $\{v\}$ . To mitigate the effect of acquisition noise and assist in DVC convergence, a mechanical regularization term  $\Phi_m^2(\{v\})$  was further considered, which measures the equilibrium gap [36] as follows:

$$\Phi_m^2(\{v\}) = \{v\}^T [K]^T [K] \{v\} \quad (3)$$

where  $[K]$  denotes the rectangular stiffness matrix associated with bulk and free-surface nodes. The weighted sum of the two aforementioned cost functions is minimized to determine the nodal displacements via regularized DVC (*i.e.*, R-DVC) as follows:

$$\{v\}_{meas} = \arg \min((\Phi_c^2(\{v\}) + \omega \Phi_m^2(\{v\}))) \quad (4)$$

where  $\omega$  is the regularization weight proportional to the regularization length  $\ell_{reg}$  raised to the power 4 [37]. To stabilize discontinuities induced by damaged (*i.e.*, cracked) regions, a damage variable  $D \in [0, 1]$  [38] was applied to reduce the regularization weight placed on the damaged elements [39]. The elementary stiffness then reads as follows:

$$[K_D^e] = [K^e](1 - D) \quad (5)$$

where  $[K^e]$  and  $[K_D^e]$  are the original and corrected elementary stiffness matrices, respectively. Such a DVC approach is referred to as regularized DVC with damage (*i.e.*, RD-DVC). To achieve element-based damage quantifications [40], mesh refinement was performed in the damaged regions, and a master-slave algorithm was used to deal with hanging nodes [41] as non-conforming meshes were constructed. Such a scheme is called regularized multi-mesh damaged DVC (*i.e.*, RMD-DVC) and was based on the following five steps (Fig. 3):

- 1) The high-resolution XCT ( $\mu$ XCT) and reconstruction code were required to obtain the volumetric images of the coal samples during the *in-situ* experiments. The morphology of the microstructure (*e.g.*, fracture, matrix, and mineral) was obtained. Such natural “speckle patterns” were regarded as carriers of the deformation information, which allowed DVC calculations to be performed between the reference  $f$  and a series of deformed configurations  $g$ .
- 2) Meshes made of eight-noded cubes (C8) were generated in the entire ROI. Overall, the mesh size, defined as the length of C8 elements, was not too small considering the computational cost (*e.g.*,  $\ell = 20$  vx). Subsequently, R-DVC was run using the so-called “relaxation” process [42] to obtain gray level residuals [43] (or DVC residuals), which highlight the low-quality registration regions (*e.g.*, fractures) as a function of the regularization length.
- 3) According to the gray-level residuals  $\rho_{dvc}$ , the damaged elements were identified, where the elementary stiffness matrix was subsequently weakened, via the damage variable  $D$ . Next, RD-DVC was run to obtain new residuals  $\rho_{dvc}$ , which should be lower than those priorly obtained.
- 4) Mesh refinement was performed on the damaged regions. Combined with the previous residuals  $\rho_{dvc}$ , highly fine-fracture morphologies were obtained. To prevent hanging nodes from being damaged, a mesh refinement extrapolation was applied.
- 5) Finally, RMD-DVC was carried out to measure the internal kinematic fields (*i.e.*, displacements, strains, and FODs/FCDs).

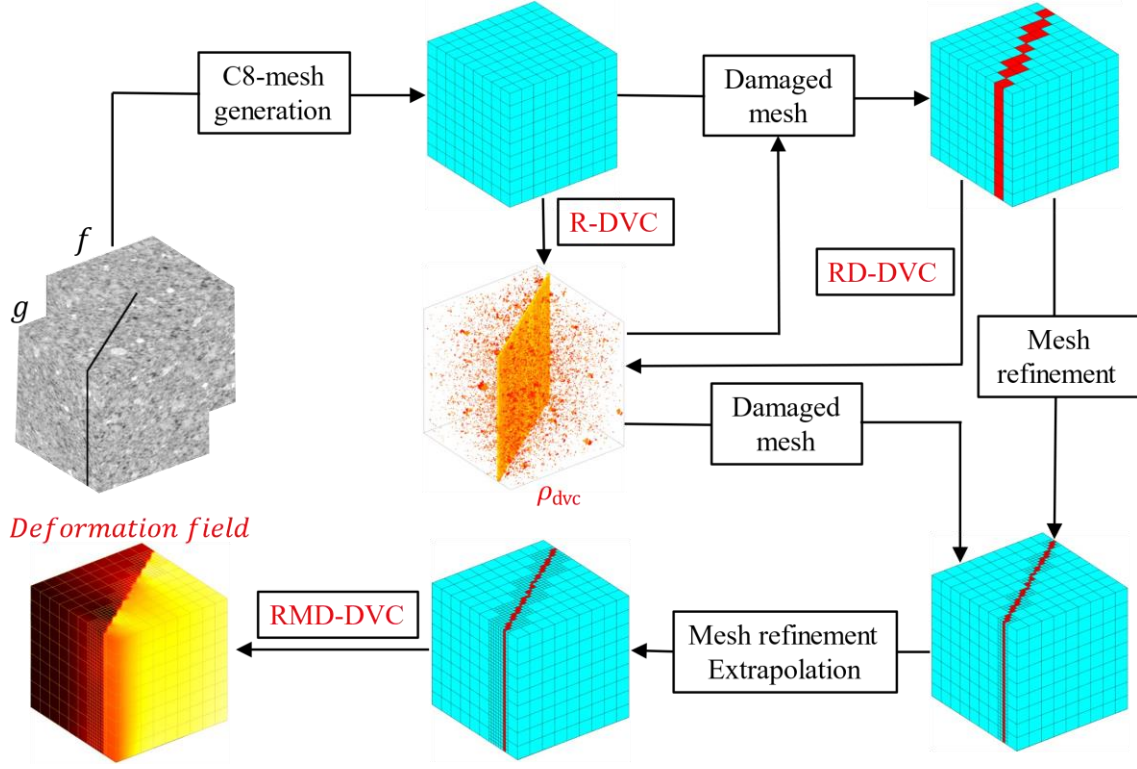


Fig. 3 Schematic representation of the regularized multi-mesh damaged-digital volume correlation (RMD-DVC) scheme for internal kinematic measurements in the presence of fractures[30, 44].

### 3. 2 Quantitative assessment parameters of fractures

#### 3.2.1 Normalized gray level residual

To evaluate the fracture activity at the voxel level, a dimensionless parameter, that is, the normalized gray-level residual  $\tilde{\rho}_{dvc}$  was used thus:

$$\tilde{\rho}_{dvc} = \frac{f - g_c}{\Delta f} \quad (7)$$

where  $f$  is the reference volume;  $g_c$  is the corrected volume by the measured displacement  $u(x, \{v\})$ ; and  $\Delta f$  is the gray level dynamic range of  $f$ .

#### 3.2.2 Fracture opening/closure displacement

In the presence of fractures, it was assumed that contributions of the main fracture opening/closure in uniaxial compression and fracture opening in triaxial compression are associated with mode I regimes; therefore, the mean FOD/FCD in each element is

approximately expressed as follows:

$$\mu_{FOD} \approx \ell \varepsilon_1 \quad (8)$$

$$\mu_{FCD} \approx \ell \varepsilon_3 \quad (9)$$

where  $\ell$  is the element size; and  $\varepsilon_1$  and  $\varepsilon_3$  are the maximum and minimum principal strains of each element, respectively. Thresholds of FOD/FCD were defined as a factor  $k$  (here,  $k = 5$  was used) times the standard FOD/FCD uncertainty quantified from experimental data (*i.e.*, two scans of the reference configuration), which were acquired prior to the analyzed tests.

### 3.2.3 Fracture volume, volume fraction and mean fracture opening/closure displacements

According to the element size and number of damaged elements with fractures, the corresponding fracture volume is expressed as follows:

$$V_f = N_d (\ell s)^3 \quad (10)$$

where  $V_f$  is the fracture volume in physical units;  $N_d$  is the number of damaged elements;  $\ell$  is the element size; and  $s$  is the scale factor from voxel to physical units. The corresponding fracture volume fraction  $\phi_f$  is then defined as follows:

$$\phi_f = \frac{V_f}{V_t} \quad (11)$$

where  $V_t$  is the total ROI volume. The mean crack opening/closure displacements (*i.e.*,  $\bar{\mu}_{FOD}$ , or  $\bar{\mu}_{FCD}$ ) are defined as follows:

$$\bar{\mu} = \frac{\sum \mu_d}{N_d} s \quad (12)$$

where  $\mu_d$  is the FCD/FOD of each damaged element.

### 3.2.4 Effective fractal dimension of fractures

Fractal dimension is an important indicator for characterizing the complexity and irregularity of coal fractures [45]. In general, the larger the fractal dimension is, the more complex the fracture structures are. The box dimension method is easy to implement, suitable for computing the fractal dimensions of fractures, and has an intuitive physical meaning [46]. The effective fractal dimension  $F_d$  is expressed thus [18]:

$$F_d = \lim_{\tau \rightarrow 0} \frac{\log N(\tau)}{\log (1/\tau)} \quad (13)$$

where  $\tau$  is the side length of the 3D box; and  $N(\tau)$  is the number of target boxes with opening/closure fractures. In the implementation, after a series of  $\tau - N(\tau)$  data were obtained, a scatter plot of the relationship between  $\log N(\tau)$  and  $\log (1/\tau)$  was considered. The slope (*i.e.*,  $F_d$ ) was then calculated via least-squares fitting.

## 4. Results and discussions

### 4.1 Artificial cracking case

An artificial cracking case was studied to evaluate the performance of the two methods of FE-based DVC and RMD-DVC. The reference and deformed volumes are shown in Fig. 4, in which the volume size was  $200 \times 200 \times 200 \text{ vx}^3$ , and an artificial crack opening of  $3 \text{ vx}$  was applied. The following two regions were defined according to the artificial crack: uncracked regions away from the crack; and cracked regions near the cracked surface. Additional Gaussian white noise was added. The standard deviation was 5% of the dynamic range of the volumes.

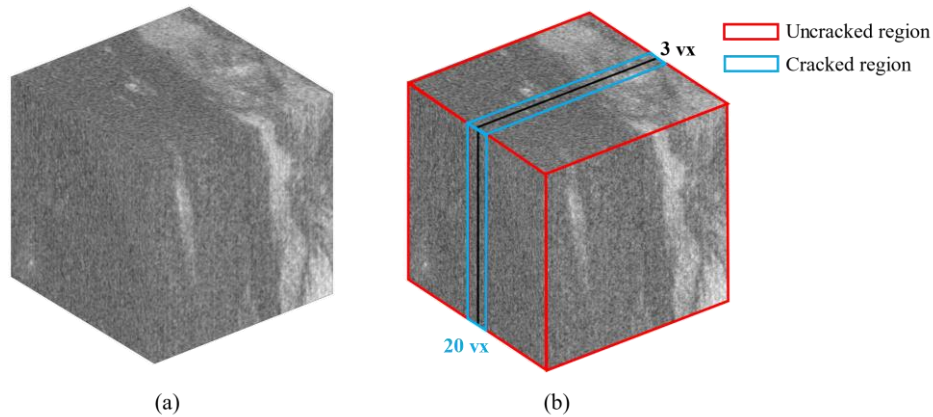


Fig. 4 Artificial cracking case: (a) the reference volume and (b) the deformed volume with an artificial crack opening of  $3 \text{ vx}$ , corrupted by Gaussian white noise with a standard deviation of 5% of the dynamic range.

The mesh size was  $20 \text{ vx}$  in FE-based DVC but  $20$  and  $4 \text{ vx}$  in the uncracked and cracked regions, respectively, for RMD-DVC. The corresponding regularization length was  $80 \text{ vx}$ , and the damage variable was equal to  $0.99$ . The standard deviations of the

displacement and maximum principal strain in the uncracked and cracked regions were quantified for the two coal samples (Table 3). Owing to its higher image quality, a lower measurement uncertainty was observed in uniaxial compression than in triaxial compression, which was consistent with the analyses reported in Table 2. For each sample, owing to the introduced schemes (*i.e.*, mechanical regularization, damage, and mesh refinement), the standard uncertainties of RMD-DVC were significantly lower than those of FE-based DVC, in particular, in the cracked region. It should be noted that the damage evaluation (*i.e.*, FOD/FOC) depends not only on the measurement uncertainty but also on the mesh scale. The performance of RMD-DVC simultaneously met these two requirements.

Table 3. Standard deviations of displacement and maximum principal strain for the two coal samples measured via DVC and RMD-DVC

Coal sample	Region	Displacement (vx)		Maximum principal strain	
		Standard DVC	RMD-DVC	Standard DVC	RMD-DVC
uniaxial	uncracked	0.113	0.006	0.0014	0.0001
	cracked	0.565	0.009	0.0020	0.0011
triaxial	uncracked	0.201	0.014	0.0032	0.0002
	cracked	0.729	0.015	0.0043	0.0021

## 4. 2 Uniaxial compression test

### 4.2.1 2D fracture network characteristics

The *in-situ* uniaxial compression test on the cuboid coal sample was analyzed in this section. The stress/strain curve is shown in Fig. 5 with CT slices (*i.e.*, the xOz plane) under different axial stresses. In these CT slices, different component densities gave rise to different gray-levels (*i.e.*, a lower density corresponded to a darker color or a lower gray-level). For the studied sample, the dark gray regions represent the coal matrix, the darkest regions highlight the fractures, and the white regions correspond to high-density minerals. A total of 12 scans were performed during the entire experiment; namely, 11 scans for pre-failure analysis (*i.e.*, loaded state) and one scan for post-failure analysis (*i.e.*, unloaded state). In the first scan, two



initial horizontal fractures were observed on the left edges (CT slice # 0), which may close with the load considering the vertical force applied. Vertical newborn fractures appeared when the sample was loaded to 20.8 MPa (CT slice # 8) and gradually developed and opened up (CT slice # 9). When the sample was loaded to 24.7 MPa, large-scale macroscopic fractures appeared (CT slice # 10) leading to the failure of the sample. Scans # 0 (cyan box) and # 9 (blue box) were used to determine the initial and newborn fracture paths, respectively.

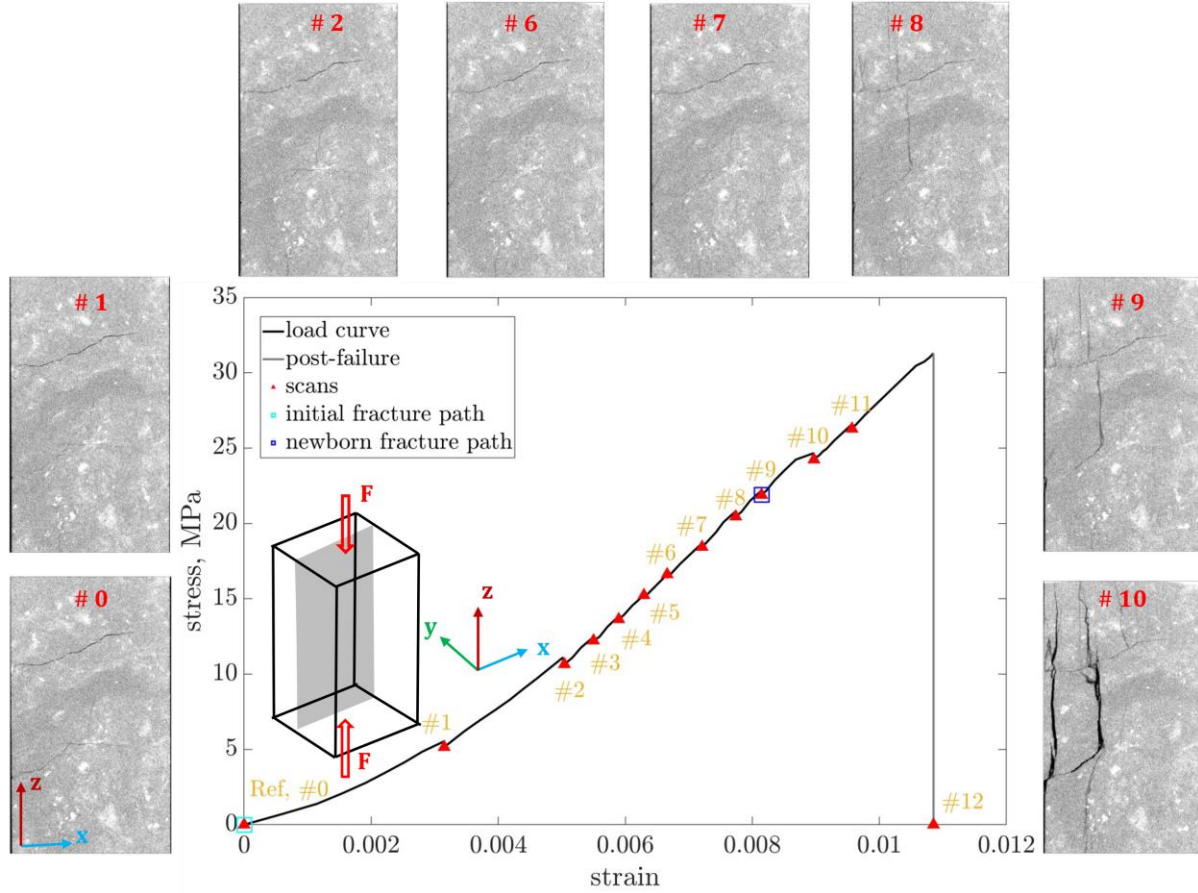


Fig. 5 Stress/strain curve for the uniaxial compression test and CT slices ( $xOz$  plane) for different load levels. The red triangles depict when the XCT scans were performed. The cyan and blue boxes depict the scans used to detect the initial and newborn fracture paths, respectively.

#### 4.2.2 Mesh and parameters in RMD-DVC analysis

To quantify the initial and newborn fractures, separated 3D meshes used in RMD-DVC were generated (Fig. 6a–b) according to the fracture features. The two main initial fractures analyzed in this section were extracted from the original scan using the Trainable Weka

Segmentation 3D of Fiji [47]; the volume fraction relative to all the initial fractures detected was approximately 85%. Such initial fractures with a horizontal spatial distribution are common in the preparation of coal samples. Newborn fractures were detected based on the gray-level residuals using R-DVC. The fine mesh corresponded to the damaged region (*i.e.*, with fractures), whereas a coarse discretization was conserved in the undamaged zones. The RMD-DVC calculation parameters were the same for all the scans (Fig. 6c). The mesh size in RMD-DVC was only 5 vx in the damaged region, which was impossible in FE-based DVC, whose mesh size is often greater than 20 vx. Therefore, the resolutions of the element-based strains or FODs/FCDs improved considerably.

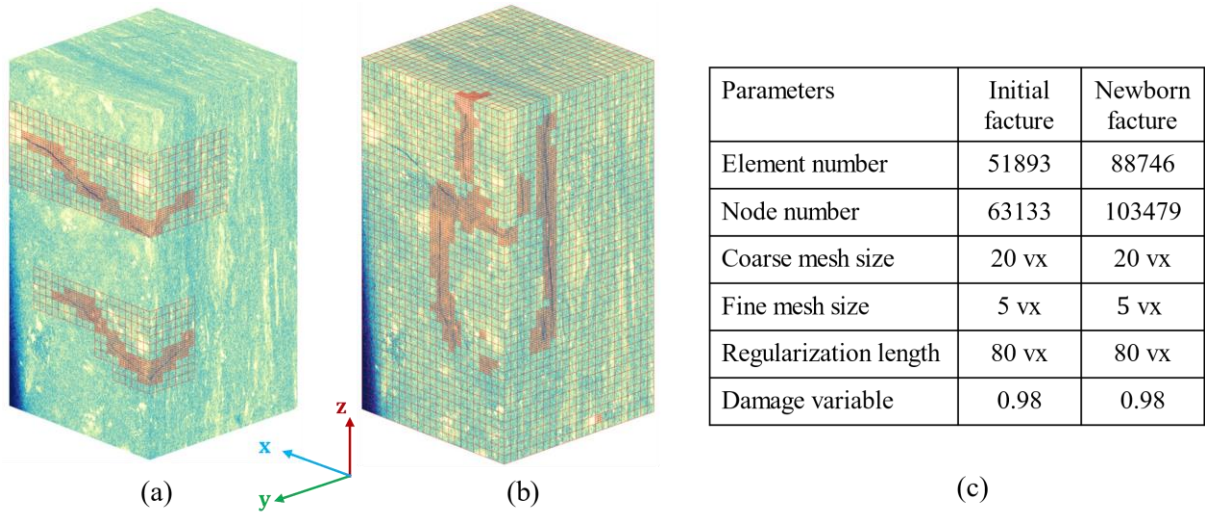


Fig. 6 3D renderings of the region of interest (ROI; parula color map) of the coal sample considered in RMD-DVC analysis. Over the chosen ROI, C8 meshes were constructed: (a) mesh for initial fractures; (b) mesh for newborn fractures; and (c) RMD-DVC calculation parameters.

#### 4.2.3 3D fracture network characteristics

To quantify the activities of 3D fracture networks in the coal samples under different axial stresses, the normalized voxel-based gray-level residual fields and element-based FOD/FCD fields were extracted from the RMD-DVC calculations. Figure 7 shows the results for the six stress levels applied before the sample failure (*i.e.*, scans # 1, 2, 6, 7, 8, and 9 in Fig. 5). Given the fact that, in the CT images, the fractures often showed extremely low gray-levels compared with other components with higher contrast, the fracture closure led to negative

residuals. Conversely, the fracture openings induced positive residuals. All normalized gray-level residuals inevitably contained acquisition noise. In addition, ring-shaped marks were observed at the top and bottom of the coal sample due to ring artifacts in the CT images during acquisition [48]. Slices with negative residuals (*i.e.*, blue hue) appeared on the left boundary of the sample loaded to 5.5 MPa, which corresponded to the closure of the initial fractures. With the increased axial stress, areas with negative residuals gradually expanded along the path of the initial fractures. At an axial stress of 20.8 MPa, positive residuals (*i.e.*, red hue) in the vertical direction were captured, which corresponded to the newborn fractures, which propagated rapidly and further opened when subjected to an axial stress of 22.2 MPa.

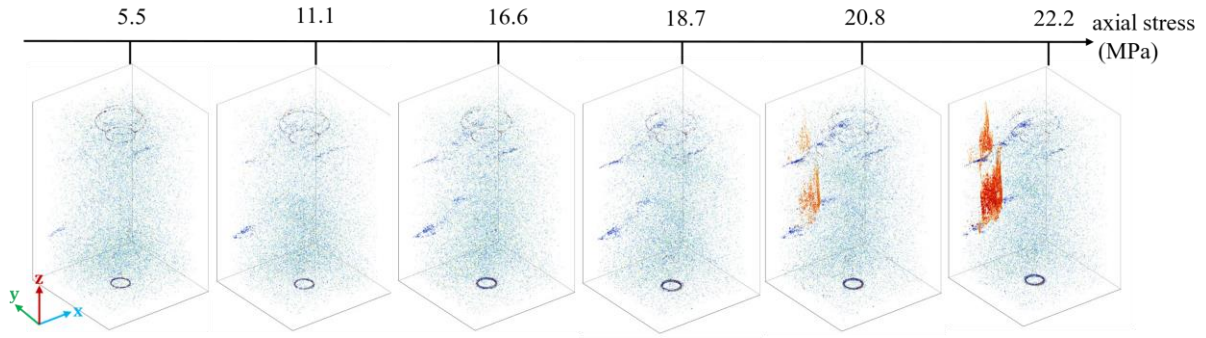


Fig. 7 Normalized voxel-based gray-level residuals for different axial stresses ( $-20\% < \tilde{\rho}_{dvc} < 20\%$ , transparent).

Figure 8 displays the estimated element-based FOD/FCD fields the stresses applied, as described in Section 3.2.2. The corresponding fracture volumes, volume fractions, and mean FCD/FOD are listed in Table 4. The used FOD and FCD thresholds were both equal to approximately  $5.6 \mu\text{m}$  (or  $0.15 \text{ vx}$ ), which was related to their standard measurement uncertainties. The fracture openings and closures are represented by the positive and negative parts of the color bar, respectively. Therefore, combined with Table 4, the entire activity of the fractures was quantitatively inferred as follows:

- (1) Before the stress level of 11.1 MPa, only the initial fractures closed but without any opening of the newborn fractures. The closed fracture volume was  $4.8 \text{ mm}^3$  ( $\phi_f = 0.5\%$ ) with a mean FCD of  $7.6 \mu\text{m}$ .
- (2) Compared with the analysis of the gray-level residuals, new phenomena were observed

for a stress level of 16.6–18.7 MPa. The newborn fractures were initiated at the boundary of the bottom initial fracture and developed along the vertical direction. The corresponding newborn fracture volume increased to 6.9 mm<sup>3</sup> (or  $\phi_f = 0.8\%$ ) with a mean FOD of 7.4  $\mu\text{m}$ . The initial fracture volume kept growing steadily, reaching 15.3 mm<sup>3</sup> ( $\phi_f = 1.7\%$ ,  $\bar{\mu}_{FCD} = 9.0 \mu\text{m}$ ). The fracture displacements remained below the CT resolution; in other words, no visible newborn fractures were observed in the CT image. Such sub-voxel levels have rarely, if ever, been revealed in other studies.

(3) At an axial stress of > 20.8 MPa, another vertical newborn fracture was initiated from the top initial fracture, which further opened and propagated at a stress level of 22.2 MPa. In this stage, the fracture volume of the newborn fractures increased to 34.7 mm<sup>3</sup>, which was greater than that of the initial fractures ( $V_f = 24.4 \text{ mm}^3$ ). The mean FOD reached 20.5  $\mu\text{m}$  compared with the mean FCD of 11.4  $\mu\text{m}$ . Similar conclusions on the investigation of fractures were found in the results of Vishal et al. [30], which verified that coal samples under uniaxial compression underwent an analogous damage process.

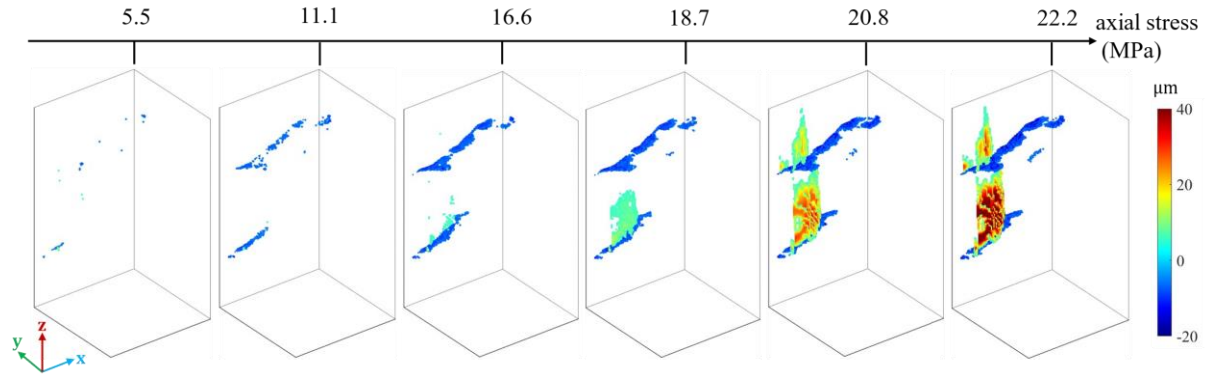


Fig. 8 Fracture opening/closure displacement (FOD/FCD) fields for different axial stresses.

Table 4. Fracture volume, volume fraction, and mean FCD/FOD for different axial stresses.

Stress (MPa)		5.5	11.1	16.6	18.7	20.8	22.2
$V_f$ (mm <sup>3</sup> )	$V_{fc}$	1.0	4.8	12.5	15.3	20.4	24.4
	$V_{fo}$	0	0	0.8	6.9	30.3	34.7
$\phi_f$ (‰)	$\phi_{fc}$	0.1	0.5	1.4	1.7	2.3	2.7
	$\phi_{fo}$	0	0	0.1	0.8	3.4	3.9

$\bar{\mu}$ ( $\mu\text{m}$ )	$\bar{\mu}_{FCD}$	7.2	7.6	8.4	9.0	10.2	11.4
	$\bar{\mu}_{FOD}$	0	0	4.7	7.4	14.7	20.5

\*notations:  $V_{fc}$  and  $V_{fo}$  are the fracture closure and opening volumes;  $\phi_{fc}$  and  $\phi_{fo}$  are the corresponding fracture closure and opening volume fractions; and  $\bar{\mu}_{FCD}$  and  $\bar{\mu}_{FOD}$  are the mean fracture closure and opening displacements, respectively.

To quantify the global activity of the fractures, the fracture volume and mean fracture displacements for the two types are shown as a function of the applied stress in Fig. 9. Three-stage growth was observed for all the curves. For the first (yellow) zone, the fracture volume and mean FCDs of the initial fractures increased gradually. No newborn fractures were initiated in this stage, which did not contribute to the fracture volume and mean FOD. The second (purple) regime corresponds to a faster increase in the fracture volume and mean FCDs/FODs for both initial and newborn fractures. Increased initial fractures closed, and newborn fractures were initiated with sub-voxel openings. The last (green) zone shows a sharp increase in the fracture volumes and mean FCDs/FODs, which induced macroscopic damage under the joint impact of the newborn and initial fractures.

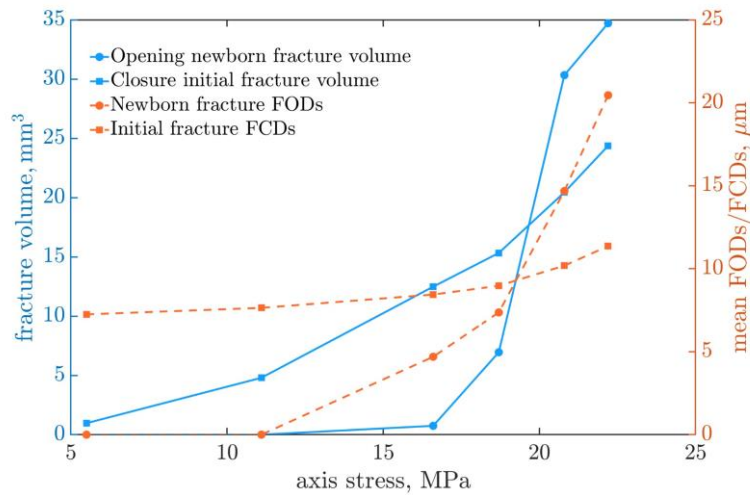


Fig. 9 Fracture volumes and mean FCDs/FODs for the initial and newborn fractures under different axial stresses.

#### 4.2.4 Effective fractal dimension and its relationship with fracture volume fraction

The effective 3D fracture networks used to calculate the fractal dimensions were produced via the element-based FCD/FOD fields (Fig. 8). The corresponding fractal dimensions  $F_d$  for the initial and newborn fractures under different axial stresses are plotted in Fig. 10a. An overall increasing trend was observed in the two curves, indicating that the complexities of the effective initial and newborn fractures became pronounced with the increasing uniaxial stress. Before the applied stress reached 18.7 MPa, the fractal dimensions  $F_d$  for the initial and newborn fractures were both less than two, pointing to the mainly planar fractures. In this stage,  $F_d$  of the initial fractures was greater than that of the newborn fractures, showing that the complexity of the closing fractures was larger than that of the opening fractures. At a stress level of  $> 18.7$  MPa, the fracture structures evolved into 3D domains as  $F_d$  of both fracture types was greater than two. In addition, a faster increase in  $F_d$  was observed for the newborn fractures than for the initial fractures. The complexity of the opening fractures was greater than that of the closing fractures.

The power-law regression (Fig. 10b) showed that the fractal dimensions of both fracture types were positively correlated with the fracture volume fractions. The exponent of the interpolation curve was larger for the newborn fractures than for the initial fractures, which demonstrated that the complexity of the newborn fractures was higher than that of the initial fractures.

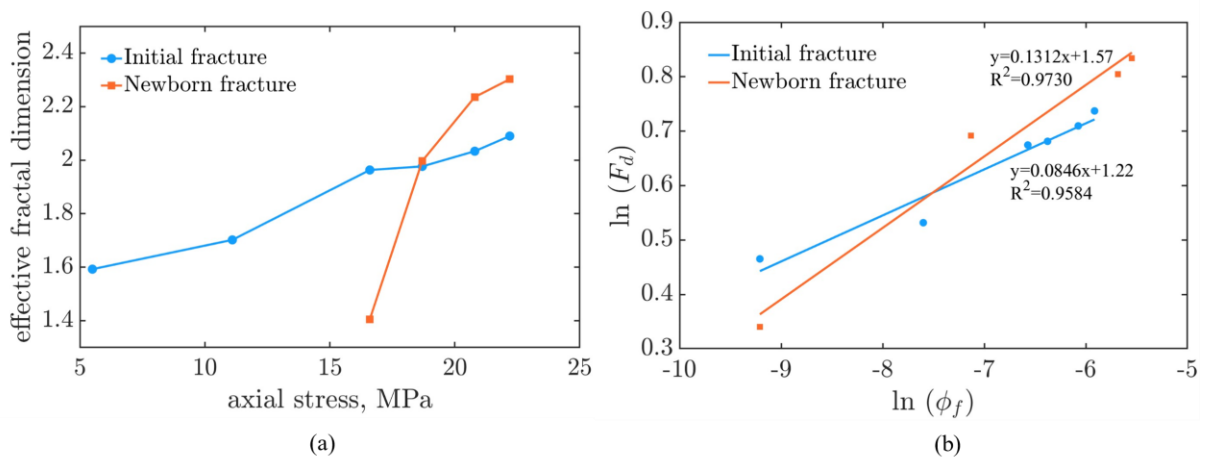


Fig. 10 (a) Effective fractal dimensions of the initial and newborn fractures and (b)



relationship between the fracture volume fraction and fractal dimension via power-law fits.

## 4. 3 Triaxial compression of coal

### 4.3.1 2D fracture network characteristics

In the triaxial compression test, the confining stress was set to 10 MPa, and the axial stresses were 18, 21, and 25 MPa. There were four scans in total: the first scan without any applied load and the other three under loading. The confining and axial stress curves versus time are plotted in Fig. 11 with the 2D CT slices (*i.e.*,  $xOy$  plane) and ortho-slices for the first and last scans. The CT images were slightly blurred owing to the casing of the pressure vessel, thereby enabling the confining pressure to be applied (with oil). Heterogeneities in the coal sample were observed on the CT slices, which mainly consisted of the coal matrix (*i.e.*, the dark gray areas), high-density minerals (*i.e.*, the light gray areas), and fractures (*i.e.*, the darkest zones). There was no visible fracture formation in the cross-section from the initial to the second stage and from the second to the last stage according to the first three 2D slices. New macroscopic fracture extensions were initiated owing to the occurrence of strain concentrations, as shown in the 2D and ortho-slices of the final scan. In this stage, the coal sample remained intact and did not undergo a catastrophic failure due to the confining pressure.

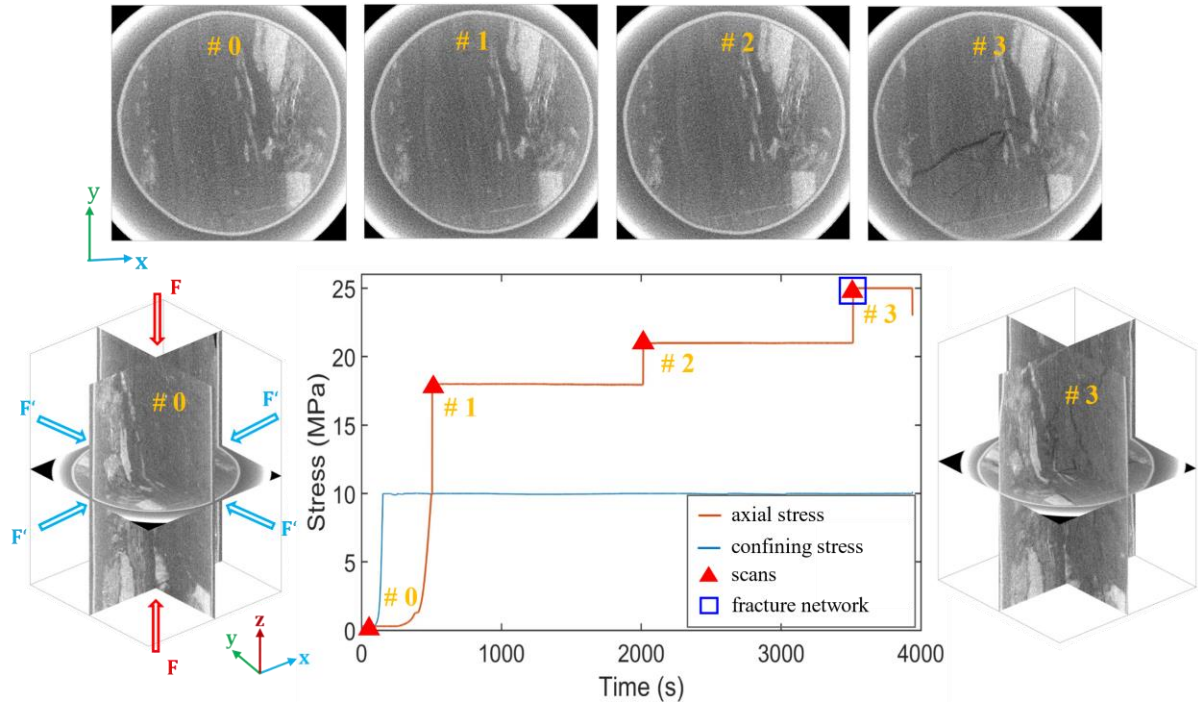


Fig. 11 Triaxial compression curves and 2D and ortho-slices of the coal sample in different loading stages. The red triangles depict when the XCT scans were performed. The blue square depicts the scan used to determine the 3D fracture network.

#### 4.3.2 Mesh and parameters in RMD-DVC analysis

The 3D mesh and its projection in the cross-section used in the RMD-DVC calculations are shown in Fig. 12a–b. To describe the fracture morphology, a fine mesh was used in regions with fractures, whereas a coarse mesh was used elsewhere. The corresponding RMD-DVC parameters are shown in Fig. 12c. In addition, increased high-density phases were observed in the left part of the sample (Fig. 12), which highlighted the heterogeneous microstructure of the coal.



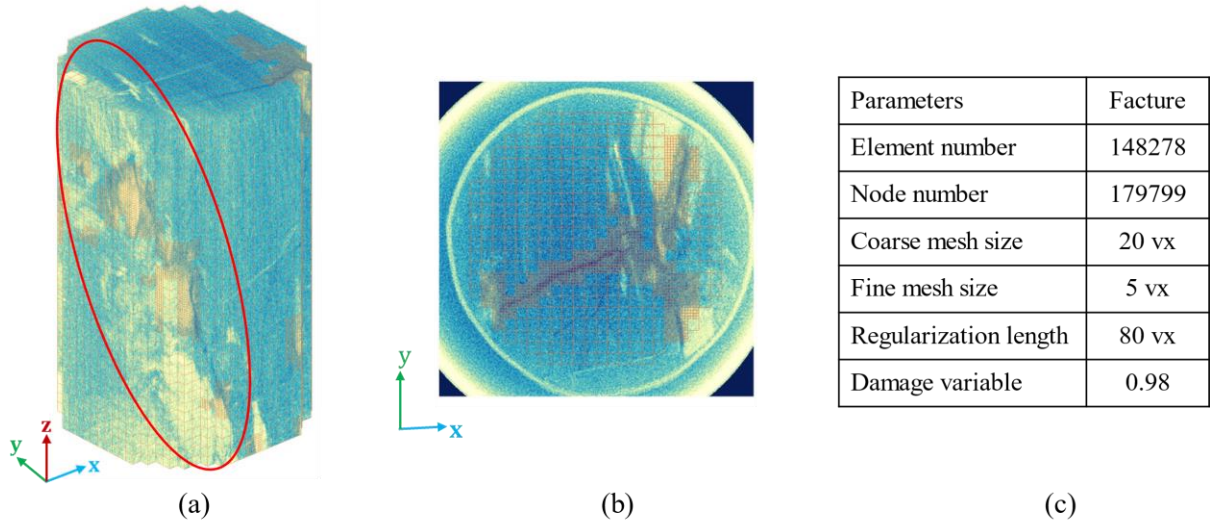


Fig. 12 3D rendering of the ROI (parula color map) of the coal sample in the last scan of the RMD-DVC analysis. Over the chosen ROI, FE-based meshes were constructed: (a) 3D mesh, where the red dashed zone depicts the high-density phases; (b) projected mesh (*i.e.*,  $xOy$  middle slice); and (c) RMD-DVC calculation parameters.

#### 4.3.3 3D fracture network characteristics

In the complete triaxial compression test, RMD-DVC analysis provided normalized voxel-based gray-level residual fields, element-based FOD fields, and element-based volumetric strain fields (Figs. 13–15, respectively). The FOD and volumetric strain thresholds were set to  $9.0 \mu\text{m}$  (or  $0.18 \text{ vx}$ ) and  $0.035$ , respectively. The corresponding fracture volume, fracture volume fraction, and mean FODs are reported in Table 5.

From the residuals shown in Fig. 13, no damage occurred before an axial stress of  $21 \text{ MPa}$ , and only extremely low residuals were observed, corresponding to various sources of uncertainty. At an axial stress of  $25 \text{ MPa}$ , macroscopic damage occurred in the complex triaxial stress environment, because increased gray-level residuals (*i.e.*, red colored regions) corresponding to strain concentrations were observed. Conversely, a small region with decreased gray-level residuals (*i.e.*, blue-colored regions) was also observed, which may represent strained bands.

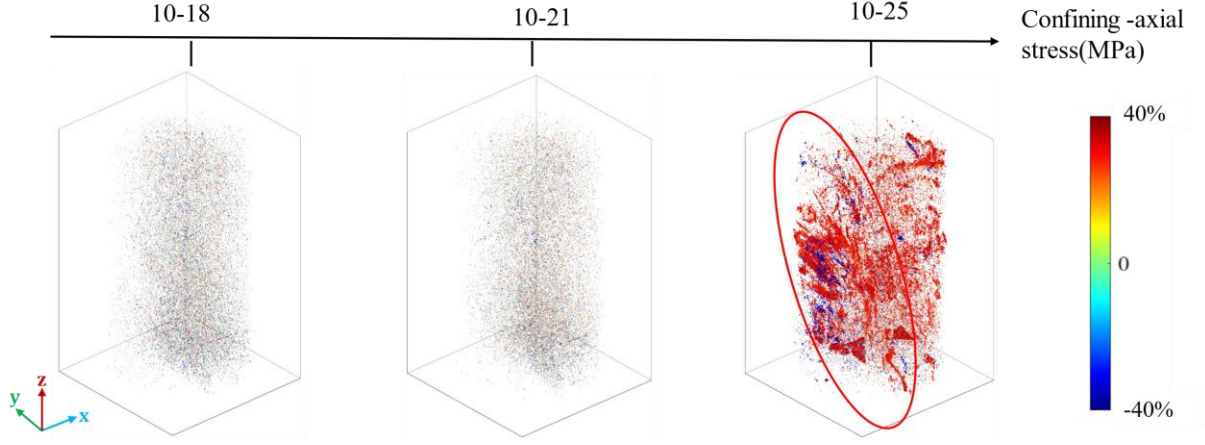


Fig. 13 Normalized voxel-scale gray-level residuals for different confining-axial stresses. ( $-20\% < \tilde{\rho}_{dvc} < 20\%$ , transparent). The red dashed zone depicts the high-density phases.

The FOD fields displayed in Fig. 14 and the results in Table 5 quantitatively revealed the formation of a 3D fracture network at the sub-voxel-to-voxel levels of FOD, which were barely observed in the gray-level residuals. Microscopic fractures were mainly initiated from the boundary of the coal sample in the early loading stage (10–18 MPa) with a fracture volume of  $13.9 \text{ mm}^3$  (or  $\phi_f = 0.9\%$ ) and a mean FOD of  $13.8 \text{ }\mu\text{m}$ . They gradually developed and coalesced toward the interior during the intermediate loading stage (10–21 MPa). Both the fracture volume (or volume fraction) and mean FODs slightly increased to  $29.7 \text{ mm}^3$  (or  $2.0\%$ ) and  $14.9 \text{ }\mu\text{m}$ , respectively. Finally, macroscopic fractures were initiated and grew rapidly at a stress level of 10–25 MPa. In this stage, the fracture volume increased to  $169.4 \text{ mm}^3$  (or  $\phi_f = 11.2\%$ ) with a mean FOD of  $39.4 \text{ }\mu\text{m}$ . In addition, fracture surfaces were observed not only at the boundary but also in the bulk coal sample. Focusing on the FOD fields, the fracture opening was larger at the boundary than in the bulk. Most fractures occurred in the high-density phases (see red dashed boxes in Figs. 12–14). This observation confirmed that the 3D fracture network was affected by the high-density inclusions.

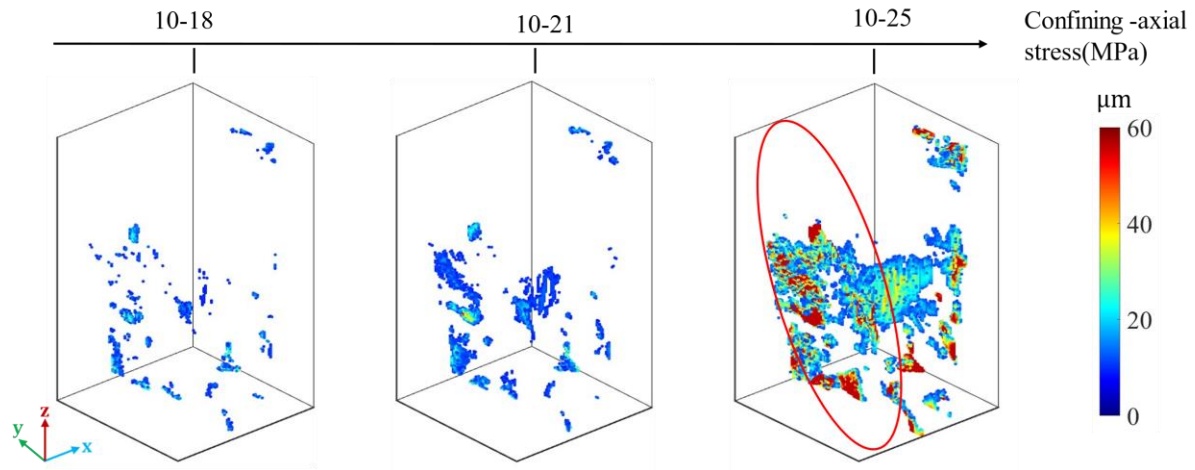


Fig. 14 FOD fields for different confining-axial stresses. The red dashed zone depicts the high-density phases.

Table 5. Fracture volume, volume fraction and mean FOD for different confining-axial stresses.

Confining-axial stress (MPa)	10-18	10-21	10-25
$V_f$ (mm <sup>3</sup> )	13.9	29.7	169.4
$\phi_f$ (‰)	0.9	2.0	11.2
$\bar{\mu}_{FOD}$ (μm)	13.8	14.9	39.4

From the volumetric strain fields (Fig. 15), at an axial stress level of < 21 MPa, the bulk volumetric strain was positive at very few locations, corresponding to the damage initiation. When macroscopic fractures appeared (10–25 MPa), the coal sample as a whole expanded, because most volumetric strains were positive. However, strained bands of mixed positive and negative levels were also observed in a small region with the high-density inclusions (see the red dashed box in Fig. 15), which illustrates that the cause of strain localization was difficult to explain in such a complex triaxial environment.

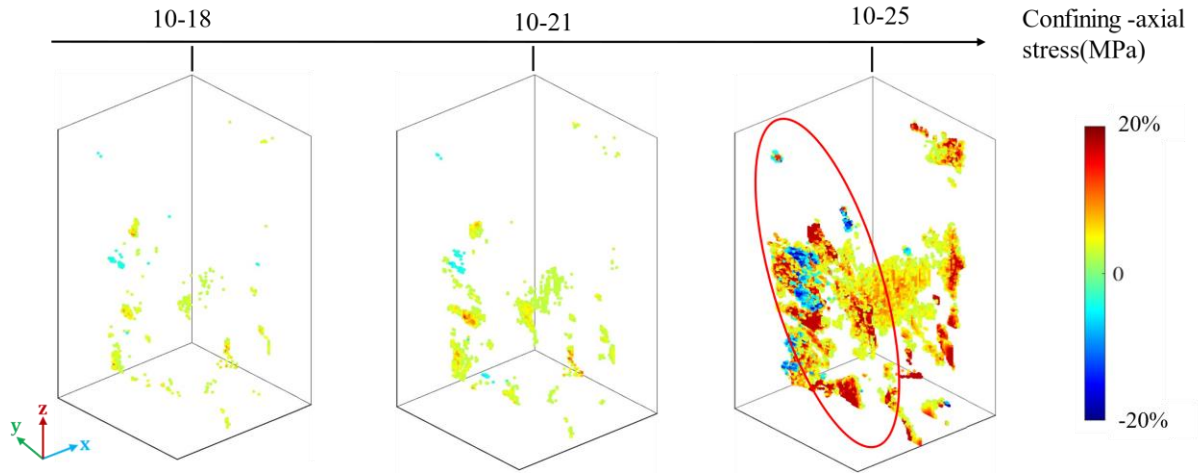


Fig. 15 Volumetric strain fields for different confining-axial stresses.

Figure 16 shows a two-stage growth in the fracture volume and mean FOD as a function of the uniaxial stress; namely, a slow increase in the early stages and then a sharper increase in the later stages. Macroscopic fractures exerted a stronger impact on the fracture volume than did microscopic fractures. Furthermore, even though the macroscopic failure was sudden, the microscopic damage was not initiated simultaneously, which demonstrated that fractures always undergo a series of processes (*i.e.*, initiation, propagation, and interaction).

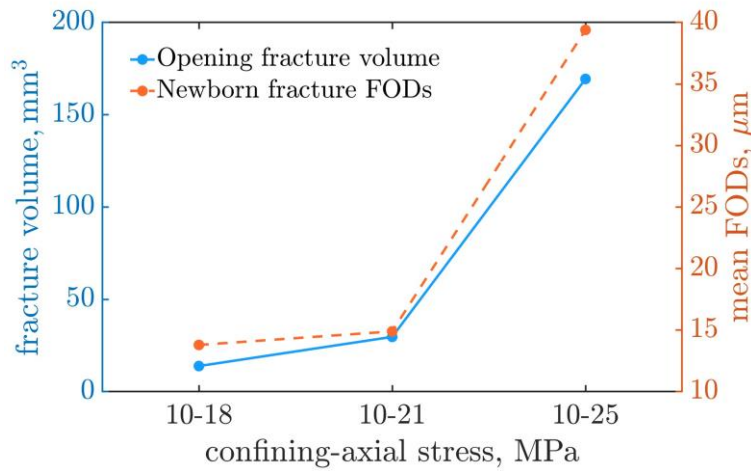


Fig. 16 Fracture volumes and mean FODs for the opening fracture network under different confining-axial stresses.

#### 4.3.4 Effective fractal dimension and its relationship with fracture rate

The FOD-based effective fractal dimension  $F_d$  with respect to the applied confining axial

stresses is shown in Fig. 17a. The dimension  $F_d$  varied within the 2–3 range, indicating that the distribution of fractures in coal was always 3D. With the increased stress, the dimension  $F_d$  also increased, showing the increased complexity of 3D fractures, in particular, in the case of macroscopic fractures (*i.e.*,  $F_d \approx 2.9$ ). The relationship between the fractal dimension and fracture volume fraction is shown in Fig. 17b. Their positive correlation was verified via the power-law interpolation.

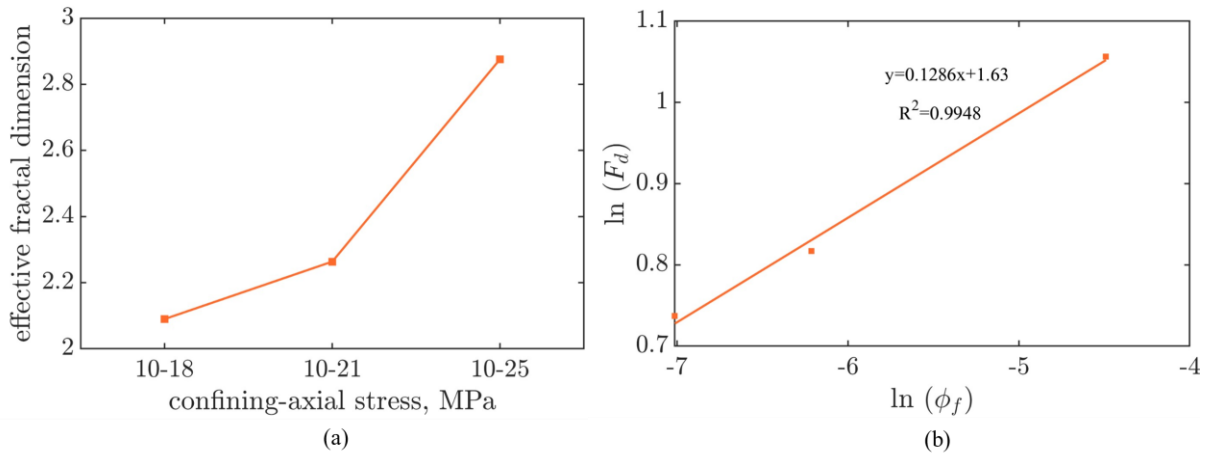


Fig. 17 (a) Effective fractal dimensions of the newborn fractures and (b) the relationship between the fracture volume fraction and fractal dimension revealed via a power-law fit.

## 5. Conclusion

This study conducted two *in-situ* experiments of uniaxial and triaxial compression on coal based on XCT. An advanced FE-based DVC analysis was utilized to quantitatively characterize the developments of the initial and newborn fractures as a function of a varying loading condition. The corresponding FODs/FCDs, volume fractions, and fractal dimensions were also assessed to investigate the damage growth characteristics. The main conclusions drawn were as follows:

- (1) The developed RMD-DVC algorithm was powerful for capturing the damage growth of coal under the varying loading modes of uniaxial and triaxial compression. The introduction of mechanical regularization, damage variables, and mesh refinement allowed for the bulk deformation measurements, in particular, for the kinematic quantification of the fractures.

- (2) In uniaxial compression, the entire damage growth process was quantified using the measured FOD/FCD fields. The detection threshold for the FOD/FCD was approximately 5.6  $\mu\text{m}$  (or 0.15 vx). In the early stages of loading (axial stress up to 11.1 MPa), 0.5 vol% initial fractures started to close from the boundary with no opening newborn fractures. At an axial stress of 16.6 MPa, 1.4 vol% initial fractures closed, and one newborn fracture was initiated at the boundary of the bottom initial fracture and gradually developed along the vertical direction with a volume fraction of 0.8% (at an axial stress of 18.7 MPa). At an axial stress of > 20.8 MPa, further closure occurred for the initial fractures, and 3.4 vol% fractures formed from coalesced and propagating microscopic fractures. Eventually, increased large-scale fractures appeared, leading to macroscopic failure.
- (3) In triaxial compression, damage was revealed via the fracture opening displacement fields. In the early stage (10–18 MPa), 0.9 vol% microscopic fractures were initiated from the boundary. In the intermediate stage (10–21 MPa), microscopic fractures propagated toward the bulk with a volume fraction of 2.0%. In the last stage (10–25 MPa), 11.2 vol% macroscopic fractures formed in the bulk coal sample. In addition, the volumetric strain fields showed mixed positive and negative zones corresponding to local contraction and expansion, which illustrated the complexity of the triaxial stress states.
- (4) The fracture parameters (*i.e.*, volume fractions and fractal dimensions) in the two *in-situ* tests were estimated from the element-based FOD/FCD fields at a sub-voxel resolution. The relationship between the fracture volume fraction and fractal dimension followed a similar trend; namely, the larger the volume fraction was, the larger the fractal dimension was, indicating the increased number of complex fractures. In addition, the fractal dimension was higher in triaxial compression than in uniaxial compression, indicating that the complexity of the fractures in the coal sample was affected by the stress conditions.
- (5) The present study allowed for the damage quantification (*i.e.*, fracture opening/closure displacement) at a sub-voxel resolution during the entire deformation process of coal. The fracture-related parameters (*i.e.*, volume fractions and fractal dimensions) were also assessed by using the refined fracture analyses, conveying a clearer physical meaning

than the traditional fracture tests.

### **Declaration of competing interest**

The authors declare that they have no known competing financial interests or personal relationships that could have appeared to influence the work reported in this paper.

### **Author Contributions**

**Haizhou Liu:** Conceptualization, Methodology, Investigation, and Writing-Original Draft.

**Lingtao Mao:** Resources, Formal analysis, Validation, Supervision and Writing-Review;

**Yang Ju:** Resources and Supervision;

**François Hild:** Conceptualization, Formal analysis, Validation, Supervision and Writing-Review.

### **Acknowledgments**

This research was funded by the National Key Research and Development Program of China (2022YFC2904102, 2022YFC3004602), Science Fund for Creative Research Groups of the National Natural Science Foundation of China (52121003), Fundamental Research Funds for the Central Universities of China (2022YJSMT04), and the China Scholarship Council.

### **Data availability**

The data that have been used are confidential.

### **Reference**

- [1] Flores RM. Coalbed methane: from hazard to resource. International Journal of Coal Geology 1998;35(1-4):3-26. [https://doi.org/10.1016/S0166-5162\(97\)00043-8](https://doi.org/10.1016/S0166-5162(97)00043-8).
- [2] Kelly KE, Wang D, Hradisky M, Silcox GD, Smith PJ, Eddings EG, et al. Underground

- coal thermal treatment as a potential low-carbon energy source. *Fuel Processing Technology* 2016;144:8-19. <https://doi.org/10.1016/j.fuproc.2015.12.006>.
- [3] Wang G, Shen J, Liu S, Jiang C, Qin X. Three-dimensional modeling and analysis of macro-pore structure of coal using combined X-ray CT imaging and fractal theory. *International Journal of Rock Mechanics and Mining Sciences* 2019;123:104082. <https://doi.org/10.1016/j.ijrmms.2019.104082>.
- [4] Wang G, Qin X, Shen J, Zhang Z, Han D, Jiang C. Quantitative analysis of microscopic structure and gas seepage characteristics of low-rank coal based on CT three-dimensional reconstruction of CT images and fractal theory. *Fuel* 2019;256:115900. <https://doi.org/10.1016/j.fuel.2019.115900>.
- [5] Li Y, Cui H, Zhang P, Wang D, Wei J. Three-dimensional visualization and quantitative characterization of coal fracture dynamic evolution under uniaxial and triaxial compression based on  $\mu$ CT scanning. *Fuel* 2020;262:116568. <https://doi.org/10.1016/j.fuel.2019.116568>.
- [6] Ward CR. Analysis, origin and significance of mineral matter in coal: An updated review. *International Journal of Coal Geology* 2016;165:1-27. <https://doi.org/10.1016/j.coal.2016.07.014>.
- [7] Wu Y, Wang D, Wei J, Yao B, Zhang H, Fu J, et al. Damage constitutive model of gas-bearing coal using industrial CT scanning technology. *Journal of Natural Gas Science and Engineering* 2022;101:104543. <https://doi.org/10.1016/j.jngse.2022.104543>.
- [8] Poulsen B, Adhikary D. A numerical study of the scale effect in coal strength. *International Journal of Rock Mechanics and Mining Sciences* 2013;63:62-71. <https://doi.org/10.1016/j.ijrmms.2013.06.006>.
- [9] Cai Y, Liu D, Pan Z, Yao Y, Li C. Mineral occurrence and its impact on fracture generation in selected Qinshui Basin coals: an experimental perspective. *International Journal of Coal Geology* 2015;150:35-50. <https://doi.org/10.1016/j.coal.2015.08.006>.
- [10] Chen H, Jiang B, Chen T, Xu S, Zhu G. Experimental study on ultrasonic velocity and anisotropy of tectonically deformed coal. *International Journal of Coal Geology* 2017;179:242-52. <https://doi.org/10.1016/j.coal.2017.06.003>.



- [11]Xie H, Ju Y, Gao F, Gao M, Zhang R. Groundbreaking theoretical and technical conceptualization of fluidized mining of deep underground solid mineral resources. *Tunnelling and Underground Space Technology* 2017;67:68-70. <https://doi.org/10.1016/j.tust.2017.04.021>.
- [12]Ramandi HL, Mostaghimi P, Armstrong RT, Saadatfar M, Pinczewski WV. Porosity and permeability characterization of coal: a micro-computed tomography study. *International Journal of Coal Geology* 2016;154:57-68. <https://doi.org/10.1016/j.coal.2015.10.001>.
- [13]Zhang R, Ai T, Li H, Zhang Z, Liu J. 3D reconstruction method and connectivity rules of fracture networks generated under different mining layouts. *International Journal of Mining Science and Technology* 2013;23(6):863-71. <https://doi.org/10.1016/j.ijmst.2013.10.013>.
- [14]Yao Y, Liu D, Cai Y, Li J. Advanced characterization of pores and fractures in coals by nuclear magnetic resonance and X-ray computed tomography. *Science China Earth Sciences* 2010;53(6):854-62. <https://doi.org/10.1007/s11430-010-0057-4>.
- [15]Liu S, Wang D, Yin G, Li M, Li X. Experimental study on the microstructure evolution laws in coal seam affected by temperature impact. *Rock Mechanics and Rock Engineering* 2020;53(3):1359-74. <https://doi.org/10.1007/s00603-019-01978-3>.
- [16]Wu Y, Wang D, Wang L, Shang Z, Zhu C, Wei J, et al. An analysis of the meso-structural damage evolution of coal using X-ray CT and a gray-scale level co-occurrence matrix method. *International Journal of Rock Mechanics and Mining Sciences* 2022;152:105062. <https://doi.org/10.1016/j.ijrmms.2022.105062>.
- [17]Shi J, Feng Z, Zhou D, Li X, Meng Q. Analysis of the permeability evolution law of in situ steam pyrolysis of bituminous coal combining with in situ CT technology. *Energy* 2022:126009. <https://doi.org/10.1016/j.energy.2022.126009>.
- [18]Sun L, Zhang C, Wang G, Huang Q, Shi Q. Research on the evolution of pore and fracture structures during spontaneous combustion of coal based on CT 3D reconstruction. *Energy* 2022;260:125033. <https://doi.org/10.1016/j.energy.2022.125033>.
- [19]Wang G, Jiang C, Shen J, Han D, Qin X. Deformation and water transport behaviors study of heterogenous coal using CT-based 3D simulation. *International Journal of Coal*

- Geology 2019;211:103204. <https://doi.org/10.1016/j.coal.2019.05.011>.
- [20] Zhou H, Zhong J, Ren W, Wang X, Yi H. Characterization of pore-fracture networks and their evolution at various measurement scales in coal samples using X-ray  $\mu$ CT and a fractal method. *International Journal of Coal Geology* 2018;189:35-49. <https://doi.org/10.1016/j.coal.2018.02.007>.
- [21] Zheng K, Qiu B, Wang Z, Li X, Li J, Gao K. Image-based numerical study of three-dimensional meso-structure effects on damage and failure of heterogeneous coal-rock under dynamic impact loads. *Particuology* 2020;51:132-41. <https://doi.org/10.1016/j.partic.2019.09.008>.
- [22] Bay BK, Smith TS, Fyhrie DP, Saad M. Digital volume correlation: three-dimensional strain mapping using X-ray tomography. *Experimental mechanics* 1999;39(3):217-26. <https://doi.org/10.1007/BF02323555>.
- [23] Buljac A, Jailin C, Mendoza A, Neggers J, Taillandier-Thomas T, Bouterf A, et al. Digital volume correlation: review of progress and challenges. *Experimental Mechanics* 2018;58(5):661-708. <https://doi.org/10.1007/s11340-018-0390-7>.
- [24] Tozzi G, Dall'Ara E, Palanca M, Curto M, Innocente F, Cristofolini L. Strain uncertainties from two digital volume correlation approaches in prophylactically augmented vertebrae: Local analysis on bone and cement-bone microstructures. *Journal of the mechanical behavior of biomedical materials* 2017;67:117-26. <https://doi.org/10.1016/j.jmbbm.2016.12.006>.
- [25] Schöberl E, Mavrogordato M, Sinclair I, Spearing S. Fibre direction strain measurement in a composite ply under pure bending using Digital Volume Correlation and Micro-focus Computed Tomography. *Journal of Composite Materials* 2020;54(14):1889-912. <https://doi.org/10.1016/j.compositesa.2020.105935>.
- [26] Chateau C, Nguyen TT, Bornert M, Yvonnet J. DVC-based image subtraction to detect microcracking in lightweight concrete. *Strain* 2018;54(5):e12276. <https://doi.org/10.1111/str.12276>.
- [27] Liu H, Mao L, Ju Y, Chiang F-p. An Adaptive and Reliable Guided Digital Volume Correlation Algorithm for Sandstone Based on 3D Scale-Invariant Feature Transform.

- Rock Mechanics and Rock Engineering 2022;55(10):6171-86.  
<https://doi.org/10.1007/s00603-022-02986-6>.
- [28] Mao L, Hao N, An L, Chiang F-p, Liu H. 3D mapping of carbon dioxide-induced strain in coal using digital volumetric speckle photography technique and X-ray computer tomography. International Journal of Coal Geology 2015;147:115-25.  
<https://doi.org/10.1016/j.coal.2015.06.015>.
- [29] Wang X, Pan J, Wang K, Mou P, Li J. Fracture variation in high-rank coal induced by hydraulic fracturing using X-ray computer tomography and digital volume correlation. International Journal of Coal Geology 2022;252:103942.  
<https://doi.org/10.1016/j.coal.2022.103942>.
- [30] Vishal V, Chandra D. Mechanical response and strain localization in coal under uniaxial loading, using digital volume correlation on X-ray tomography images. International Journal of Rock Mechanics and Mining Sciences 2022;154:105103.  
<https://doi.org/10.1016/j.ijrmms.2022.105103>.
- [31] Mao L, Liu H, Zhu Y, Zhu Z, Guo R, Chiang F-p. 3D strain mapping of opaque materials using an improved digital volumetric speckle photography technique with X-ray microtomography. Applied Sciences 2019;9(7):1418. <https://doi.org/10.3390/app9071418>.
- [32] Ju Y, Wang J, Ruidong P, Lingtao M, Liu H. Industrial CT scanning test system. Patents; 2018. <https://doi.org/patent/US9891178B2/en>.
- [33] Kak AC, Slaney M. Principles of computerized tomographic imaging: SIAM 2001.
- [34] Yokota M, Kusano T, Mori M, Okuda K, Matsunaga T. In-situ 3D visualization of compression process for powder beds by synchrotron-radiation X-ray computed laminography. Powder Technology 2021;380:265-72.  
<https://doi.org/10.1016/j.powtec.2020.11.019>.
- [35] Roux S, Hild F, Viot P, Bernard D. Three-dimensional image correlation from X-ray computed tomography of solid foam. Composites Part A: Applied science and manufacturing 2008;39(8):1253-65. <https://doi.org/10.1016/j.compositesa.2007.11.011>.
- [36] Claire D, Hild F, Roux S. A finite element formulation to identify damage fields: the equilibrium gap method. International journal for numerical methods in engineering

- 2004;61(2):189-208. <https://doi.org/10.1002/nme.1057>.
- [37] Leclerc H, Périé J-N, Roux S, Hild F. Voxel-scale digital volume correlation. *Experimental Mechanics* 2011;51(4):479-90. <https://doi.org/10.1007/s11340-010-9407-6>.
- [38] Lippmann H, Lemaitre J. *A Course on Damage Mechanics*: Springer Berlin/Heidelberg, 1992. <https://doi.org/10.1007/978-3-662-02761-5>.
- [39] Hild F, Bouterf A, Roux S. Damage measurements via DIC. *International Journal of Fracture* 2015;191(1):77-105. <https://doi.org/10.1007/s10704-015-0004-7>.
- [40] Sciuti V, Vargas R, Canto R, Hild F. Pyramidal adaptive meshing for Digital Image Correlation dealing with cracks. *Engineering Fracture Mechanics* 2021;256:107931. <https://doi.org/10.1016/j.engfracmech.2021.107931>.
- [41] Liu G-R, Quek SS. *The finite element method: a practical course*: Butterworth-Heinemann, 2013. <https://doi.org/10.1017/S0001924000097281>.
- [42] Tomičević Z, Hild F, Roux S. Mechanics-aided digital image correlation. *The Journal of Strain Analysis for Engineering Design* 2013;48(5):330-43. <https://doi.org/10.1177/0309324713482457>.
- [43] Buljac A, Shakoor M, Neggers J, Bernacki M, Bouchard P-O, Helfen L, et al. Numerical validation framework for micromechanical simulations based on synchrotron 3D imaging. *Computational Mechanics* 2017;59(3):419-41. <https://doi.org/10.1007/s00466-016-1357-0>.
- [44] Madi K, Tozzi G, Zhang Q, Tong J, Cossey A, Au A, et al. Computation of full-field displacements in a scaffold implant using digital volume correlation and finite element analysis. *Medical Engineering & Physics* 2013;35(9):1298-1312. <https://doi.org/10.1016/j.medengphy.2013.02.001>.
- [45] Yongzan W, Guanhua N, Xinyue Z, Yicheng Z, Gang W, Zhenyang W, et al. Fine characterization of pore structure of acidified anthracite based on liquid intrusion method and Micro-CT. *Energy* 2023;263:125639. <https://doi.org/10.1016/j.energy.2022.125639>.
- [46] Liang S, Xiaoqi W, Xu J, Jianming L, Songtao W. Three dimensional characterization and quantitative connectivity analysis of micro/nano pore space. *Petroleum Exploration and Development* 2016;43(3):537-46. [https://doi.org/10.1016/S1876-3804\(16\)30063-5](https://doi.org/10.1016/S1876-3804(16)30063-5).

- 1 [47]Arganda-Carreras I, Kaynig V, Rueden C, Eliceiri KW, Schindelin J, Cardona A, et al.  
2 Trainable Weka Segmentation: a machine learning tool for microscopy pixel  
3 classification. *Bioinformatics* 2017;33(15):2424-6.  
4 <https://doi.org/10.1093/bioinformatics/btx180>.
- 5 [48]Limodin N, Réthoré J, Adrien J, Buffière J-Y, Hild F, Roux S. Analysis and artifact  
6 correction for volume correlation measurements using tomographic images from a  
7 laboratory X-ray source. *Experimental mechanics* 2011;51(6):959-70.  
8 <https://doi.org/10.1007/s11340-010-9397-4>.